Improved photodegradation of anionic dyes using a complex graphitic carbon nitride and iron-based metal–organic framework material†

Huan V. Doan, [ID] ‡[ab] Hoa Thi Nguyen ‡[b] Valeska P. Ting, [ID] [c] Shaoliang Guan,[de] Jean-Charles Eloi,[a] Simon R. Hall [ID] [a] and Xuan Nui Pham [ID] *[b]

Introducing heterostructures to graphitic carbon nitrides (g-C_3N_4) can improve the activity of visible-light-driven catalysts for the efficient treatment of multiple toxic pollutants in water. Here, we report for the first time that a complex material can be constructed from oxygen-doped g-C_3N_4 and a MIL-53(Fe) metal–organic framework using facile hydrothermal synthesis and recycled polyethylene terephthalate from plastic waste. The novel multi-walled nanotube structure of the O-g-C_3N_4/MIL-53(Fe) composite, which enables the unique interfacial charge transfer at the heterojunction, showed an obvious enhancement in the separation efficiency of the photochemical electron–hole pairs. This resulted in a narrow bandgap energy (2.30 eV, compared to 2.55 eV in O-g-C_3N_4), high photocurrent intensity (0.17 mA cm^{2}, compared to 0.12 mA cm^{2} and 0.09 mA cm^{2} in MIL-53(Fe) and O-g-C_3N_4, respectively) and excellent catalytic performance in the photodegradation of anionic azo dyes (95% for RR 195 and 99% for RY 145 degraded after 4 h, and only a minor change in the efficiency observed after four consecutive tests). These results demonstrate the development of new catalysts made from waste feedstocks that show high stability, ease of fabrication and can operate in natural light for environmental remediation.

[a]School of Chemistry, University of Bristol, Bristol, BS8 1TS, UK

[b]Department of Chemical Engineering, Hanoi University of Mining and Geology, 18 Pho Vien, Duc Thang, Bac Tu Liem, Hanoi, Vietnam. E-mail: phamxuannui@humg.edu.vn

[c]Department of Mechanical Engineering, University of Bristol, Bristol, BS8 1TR, UK

[d]School of Chemistry, Cardiff University, Cardiff, CF10 3AT, UK

[e]HarwellXPS, Research Complex at Harwell, Rutherford Appleton Laboratory, Didcot, OX11 0FA, UK

‡ Joint rst authorship: both authors contributed equally to this work.

1. Introduction

Graphitic carbon nitrides (g-C_3N_4) have attracted much attention recently due to their photocatalytic activity over a wide range of wavelengths with a distinctive 2D structure and high stability.[22,23] Most recent studies have been directed towards the development of g-C_3N_4 with diverse morphologies such as nanoparticles,[24] nanotubes,[25] nanorods[26] and nanowires.[27] These different morphologies are achieved through the use of various solvents such as water, acetone, N-methyl pyrrolidone and ethanol, or through the pyrolysis of various nitrogen-rich precursors such as urea, thiourea, cyanamide, dicyandiamide and melamine.[28,29] Doping g-C_3N_4 with non-metallic elements (such as O, S and P) has also been used to tune the electronic structure towards increased visible light absorption.[30] In addition, creating defective frameworks can improve the separation efficiency of the photochemical electron−hole pairs, thus improving [30–33] the photocatalytic activity of this material. The synthesis of oxygen-doped graphitic carbon nitride (O-g-C_3N_4) was first reported by Li et al.,[34] showing that the oxygen in the g-C_3N_4 lattice could induce intrinsic electronic and band structure modulation, resulting in an absorbance edge of 498 nm and enhanced visible-light photoactivity. Pham et al. also reported the synthesis of an O-g-C_3N_4/H-ZSM-5 composite with an improved catalytic performance for Reactive Red 195 (RR 195) dye photodegradation.[35] The results show that with 40 wt% doped oxygen, the composite had a comparatively high surface area of 259 m^2 g^{-1}, a narrow bandgap energy of 2.62 eV, enhanced photocatalytic activity (more than 96% of RR 195 removed a er 5 h under natural light), remarkable stability and long-term recyclability (the photodegradation efficiency of RR 195 remained above 91% a er 4 cycles).

The heterostructure construction created by the interface between g-C_3N_4 and other porous materials can increase the surface electrostatic interactions, achieve unique porosity and morphologies, and can limit the recombination of photo-generated electron−hole pairs, and is thus of broad and current interest.[36–38] To

this extent, metal–organic frameworks (MOFs) with diverse chemical composition tions, exceptional surface areas and tuneable porosities,[39–42] have gained increasing attention in recent years. The heterojunctions in composites of g-C_3N_4 with MOFs, formed by the p–p interactions between the aromatic and the triazine rings, can accelerate the charge transfer across the interface and shorten the charge transport distance, thus enhancing the separation rates of photoinduced electron–hole pairs.[43] Huang et al. have reported a hybrid composite based on MIL-53(Fe) and g-C_3N_4, showing that the composite exhibited an enhanced separation and migration rate of the photo-induced charges, resulting in excellent visible light-responsive photocatalytic activity for the reduction of Cr(VI).[44] MIL-101(Fe)/g-C_3N_4 heterojunction hybrids were also prepared via the in situ growth of MIL-101(Fe) onto a g-C_3N_4 surface.[45] These composites, with enhanced light absorption and efficient charge carrier separation, were employed as bifunctional photocatalysts for the simultaneous reduction of Cr(VI) and degradation of bisphenol-A (BPA), exhibiting a clear enhancement in photocatalytic activity compared to either MIL-101(Fe) or g-C_3N_4 alone. Similar results were also reported for the development of g-C_3N_4/NH_2-MIL-101(Fe) for Cr(VI) reduction and methyl orange degradation[46] and g-C_3N_4/NH_2-MIL-88B(Fe) for methylene blue degradation.[47] The direct excitation of the extensive iron–oxo (Fe–O) clusters in MIL-53(Fe), MIL-101(Fe) and MIL-88B(Fe) has demonstrated that these MOFs can be employed as exceptional candidates for the preparation of visible-light-driven catalysts to generate holes and hydroxyl radicals for the efficient treatment of multiple toxic pollutants in water.[48,49]

The aim of this work was to develop a novel and low-cost photocatalyst for the removal of azo dyes. This involved the construction of a complex O-g-C_3N_4 and MIL-53(Fe) MOF material to take advantage of the excellent properties of both components in reducing the rate of electron–hole recombination in photo-catalysis. The sample preparation was based on inexpensive chemicals including urea and abundant iron precursors. In this study, we also proposed the use of terephthalic acid (TPA or 1,4-benzenedicarboxylic acid) produced directly from polyethylene terephthalate (PET) in waste plastic bottles to explore new and cheaper sources of starting materials for the economical production of MOF materials. The degradation of two commercial textile anionic azo dyes (RR 195 and Reactive Yellow 145, RY 145) was subsequently used to investigate the photocatalytic activity of the O-g-C_3N_4/MIL-53(Fe) composite.

2. Experimental

2.1. Preparation of oxygen doped graphitic carbon nitride (O-g-C_3N_4)

The synthesis of graphitic carbon nitride (g-C_3N_4) and oxygen doped graphitic carbon nitride (O-g-C_3N_4) was carried out according to our reported procedure[35] using urea ((NH_2)$_2$CO) as a precursor. Typically, 9 g of urea was directly heated at 550 C for 2 h with a heating rate of 2 C min^{-1} to obtain g-C_3N_4. In the synthesis of O-g-C_3N_4, oxygen was doped by the addition of hydrogen peroxide (H_2O_2), as seen in Scheme 1. First, 9 g of urea was dispersed in 40 ml of H_2O_2, magnetically stirring at 300 rpm for 30 min at room temperature. A er drying at 60 C for 12 h, the solid was placed in a furnace and calcined under air at 550 C for 2 h at a heating rate of 2 C min^{-1} to obtain O-g-C_3N_4.
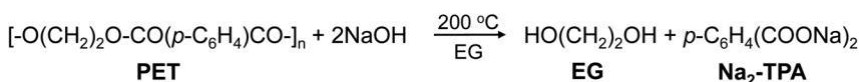
.
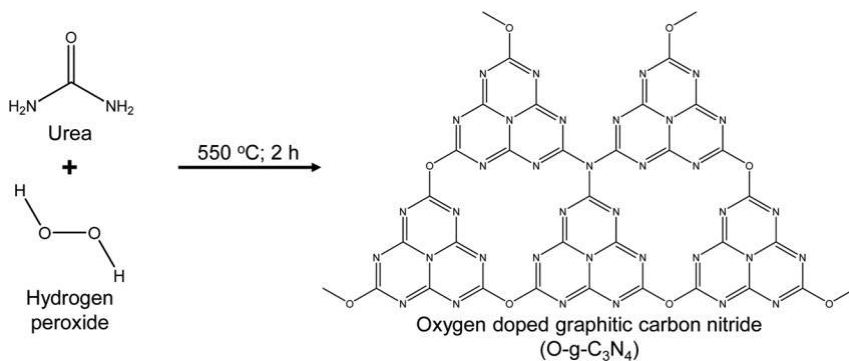
Scheme 1 Synthesis of O-g-C3N4 from urea and hydrogen peroxide. The structure of O-g-C3N4 was proposed by Wei et al.[50]

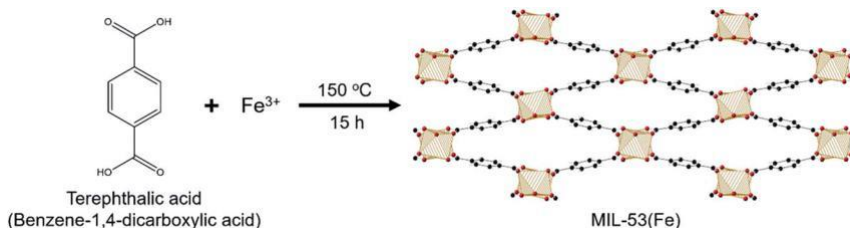## 2.2. Preparation of terephthalic acid from plastic waste

In this study, PET water bottles randomly collected from recycling facilities were used as a source of plastic waste to prepare terephthalic acid. A er removing the caps and labels, these water bottles were cleaned, dried and cut into small pieces of 5 5 mm. TPA was synthesised by the alkali decomposition of waste PET with sodium hydroxide (NaOH) in ethylene glycol (EG), as seen in Scheme 2. First, a mixture of 12 g waste PET, 22 g NaOH and 55 ml EG was added to a 500 ml 3-neck round-bottom ask with a serpentine condenser, then magnetically stirred at 300 rpm and heated at 190 C for 3 h. A er that, the reactor containing a milky solution was cooled down to 80 C and 200 ml distilled water was added under stirring to dissolve the mixture completely. Unreacted plastic pieces were separated from the reaction by vacuum filtration with filter paper.

The aqueous filtrate solution was acidified to pH 3 with 2 M sulphuric acid (H_2SO_4) to achieve precipitation. The white solid was filtered and washed with distilled water 3 times to eliminate the sodium sulphate, before drying in an oven at 60 C to obtain the pure TPA powder (dried weight ¼ 6 g).

2.3. Preparation of MIL-53(Fe)

The MIL-53(Fe) MOF was prepared by a solvothermal reaction, as illustrated in Scheme 3. First, 1.35 g of iron(III) chloride hexahydrate ($FeCl_3$$6H_2O$) and 0.83 g of TPA were added in 25 ml of dimethylformamide (DMF), magnetically stirring at 300 rpm for 30 min at room temperature to obtain a stock solution. This mixture was then transferred to a 100 ml Te on-lined stainless-steel autoclave and placed in an oven, which was heated at 150 C for 15 h. A er crystallisation, the resultant precipitate was separated from the solution by centrifugation (3000 rpm for 10

$$[-O(CH_2)_2O-CO(p-C_6H_4)CO-]_n + 2NaOH \xrightarrow[EG]{200\ °C} HO(CH_2)_2OH + p-C_6H_4(COONa)_2$$

PET   EG   Na$_2$-TPA

Scheme 2 Alkali decomposition of polyethylene terephthalate with sodium hydroxide in ethylene glycol.

Scheme 3 Schematic illustration of MIL-53(Fe) synthesis. C atoms are represented by the black spheres. O atoms are represented by the red spheres. Iron clusters are represented by the stripe-filled solids.

min), washed three times with ethanol and dried at 60 C for 12 h to obtain a yellowish-orange MIL-53(Fe) solid.

2.4. Preparation of O-g-C$_3$N$_4$/MIL-53(Fe)

The O-g-C$_3$N$_4$/MIL-53(Fe) composite was prepared by adding 10 ml DMF solution containing 0.25 g of O-g-C$_3$N$_4$ to 25 ml of the MIL-53(Fe) stock solution containing 1.35 g of FeCl$_3$$6H$_2$O and 0.83 g of TPA under stirring at 300 rpm for 30 min at room temperature. The mixture was transferred to the autoclave and subsequent steps followed the synthesis of MIL-53(Fe) in Section 2.3.

2.5. Photodegradation of anionic dyes

The photocatalytic activity of the g-C$_3$N$_4$, O-g-C$_3$N$_4$, MIL-53(Fe) and O-g-C$_3$N$_4$/MIL-53(Fe) samples was assessed for the degradation of RR 195 and RY 145 under solar irradiation between 10 am and 2 pm at room temperature. In a typical experiment, 50 mg of the photocatalyst was dispersed in 40 ml of an aqueous solution containing the anionic dyes (50 ppm). Prior to the reaction, the above mixture was magnetically stirred at 300 rpm in the dark for 60 min to achieve the adsorption– desorption equilibrium, and the initial concentration (C_o) was taken at this point. A er every hour (up to 5 h in this study), a small quantity of the supernatant was taken and analysed under a UV-Vis spectrometer to record the concentration (C) and calculate the dye degradation using eqn (2) in the ESI.† The degradation of

RR 195 was tested without catalysts to estimate the baseline during the experiment. A xenon lamp (500 W) was also used in the removal of RR 195 over O-g-C$_3$N$_4$ to compare with the corresponding experiment under natural sunlight. The performance of the O-g-C$_3$N$_4$/MIL-53(Fe) composite material in the photo-degradation of anionic dyes was systematically investigated by varying the amount of the catalyst (25–75 mg) and the concentration of RR 195 and RY 145 (30–70 ppm) while the other conditions remained unchanged.

3. Results and discussion

3.1. Structural properties

The crystal and chemical structures of the synthesised materials, including g-C$_3$N$_4$, O-g-C$_3$N$_4$, MIL-53(Fe) and O-g-C$_3$N$_4$/MIL-53(Fe), were revealed using powder

X-ray diffraction (PXRD) and Fourier-transform infrared (FT-IR) spectroscopy. The results are shown in Fig. 1.

As can be seen in Fig. 1a, two typical peaks of graphitic carbon nitride,[22,51] at 27 and 13 degrees 2-theta are observed in the g-C3N4 sample, corresponding to the stacking of carbon nitride sheets (002) and the in-plane ordering of polymeric melon units (100), respectively. In the oxygen doped sample (O-g-C3N4), the peak at 27 degrees 2-theta is much weaker and broader, indicating less long-range order of graphitic stacking. It can also be noticed that this peak is slightly shifted to a lower angle, which is due to the increase of the interlayer distance in O-g-C3N4. Additionally, the peak at 13 degrees 2-theta almost disappears in this sample, which is ascribed to the decreased planar size of the layers. The FT-IR spectra (Fig. 1b) demonstrate that the stretching vibrations of N−H (evidenced by the broad absorption bands between 3100 and 3300 cm^{-1}), C]N (evidenced by the two peaks at 1574 and 1638 cm^{-1}) and C−N in the aromatic ring (evidenced by the further three peaks between 1200 and 1500 cm^{-1}) were retained in the structures of all of the graphitic carbon nitride samples. A sharp peak can also be noted at 891 cm^{-1}, indicating the appearance of the triazine ring in these samples.[52] The peak at 1238 cm^{-1} for the stretching vibration of C−O−C overlaps with the peak at 1242 cm^{-1} for the stretching vibration of C−N, thus is difficult to notice in O-g-C3N4. However, the increased intensity of these peaks, together with
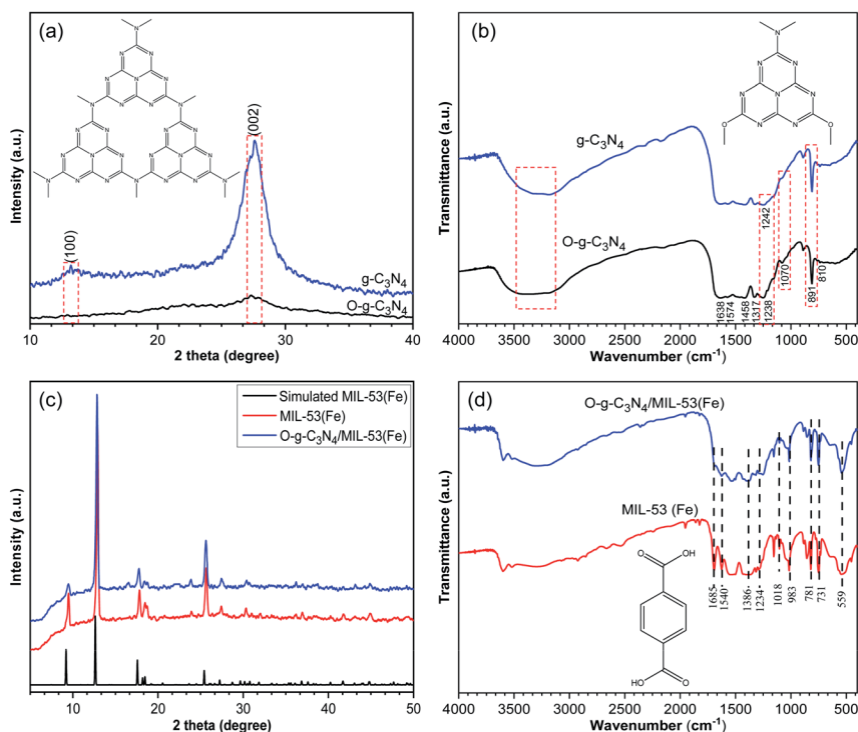

Fig. 1 (a) PXRD patterns and (b) FT-IR spectra of g-C3N4 and O-g-C3N4. (c) PXRD patterns of the simulated MIL-53(Fe), as-synthesised MIL-53(Fe) and O-g-C3N4/MIL-53(Fe). (d) FT-IR spectra of MIL-53(Fe) and O-g-C3N4/MIL-53(Fe).

a new peak at 1070 cm[1], demonstrate the existence of C–O bonds in the oxygen-doped sample.[50]

In this study, TPA recycled from PET waste was used as the organic ligand in the synthesis of MIL-53(Fe). In the PXRD pattern (Fig. 1c), all of the main peaks for the simulated MIL-53(Fe),[53] including those at 9, 13, 17, 19 and 26 degrees 2-theta, are observed in the synthesised MIL-53(Fe) and O-g-C3N4/MIL-53(Fe). This result demonstrates that MIL-53(Fe) crystals were successfully formed using the recycled TPA and that the MOF crystallinity was maintained during the facile synthesis of the novel O-g-C3N4/MIL-53(Fe) composite. The FT-IR spectrum of the O-g-C3N4/ MIL-53(Fe) composite (Fig. 1d) con rms that all of the bonding groups of MIL-53(Fe) are retained, including the stretching vibration of C–H in the aromatic ring (731 cm[1]),[54] COO– in the dicarboxylate group (1685, 1540 and 1386 cm[1])[55] and Fe–O in the bonding between Fe(III) and the carboxylic group (559 cm[1]). A decreased intensity of the peak at 1685 cm[1] in O-g-C3N4/MIL-53(Fe) compared to MIL-53(Fe) might be due to the integration of the graphitic carbon nitride into the composite material. A similar result in MIL-101(Fe)/g-C3N4 was reported by Zhao et al.[45]

X-ray photoelectron spectroscopy (XPS) was conducted to investigate the elemental valence states and composition of the O-g-C3N4/MIL-53(Fe) composite sample (Fig. 2a–d). In the high-resolution C 1s spectrum (Fig. 2b), the three peaks at 284.8, 287.6 and 289.3 eV can be assigned to graphitic carbon (sp^3 C), sp^2-bonded carbon (N]C–N) and the C atoms bonded with O (C–O), respectively.[56]
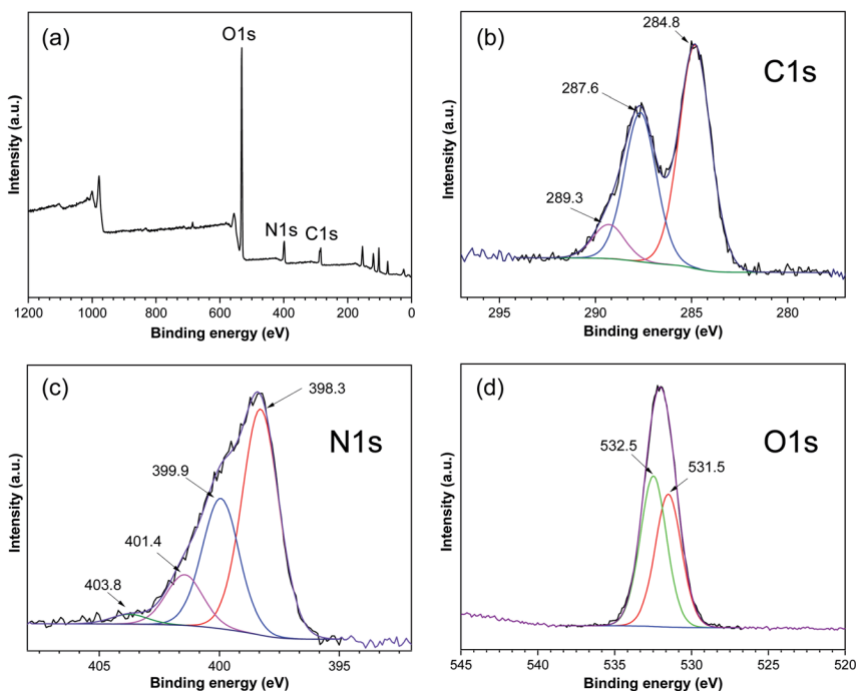

Fig. 2 XPS (a) survey scan, (b) C 1s, (c) N 1s and (d) O 1s spectra of the O-g-C3N4/MIL-53(Fe) composite.

The N 1s spectrum of this sample can be fitted using four peaks at 398.3, 399.9, 401.4 and 403.8 eV, which correspond to sp^2 N (C−N]C), tertiary N atoms (sp^3 N), amino-functional groups (C$_2$−N−H) and p excitation, respectively.[57] These results con rm that graphitic carbon nitride was formed and indeed combined closely with the MOF. In addition, the O 1s spectrum can be divided into two peaks at 531.5 and 532.5 eV, which correspond to the adsorption of water and N−C−O, respectively, [58,59] confirming that oxygen was successfully doped in the graphitic carbon nitride using urea and hydrogen peroxide as precursors.

3.2. Textural properties

The morphologies and elemental compositions of MIL-53(Fe), O-g-C$_3$N$_4$ and the O-g-C$_3$N$_4$/MIL-53(Fe) composite were analysed by scanning electron microscopy (SEM), energy-dispersive X-ray spectroscopy (EDX) and transmission electron microscopy (TEM).

Fig. 3a shows that the MOF crystals are unevenly rod-shaped with the lengths varying between 0.5 and 2 mm, which is consistent with the observation of MIL-53(Fe) reported previously.[60] Graphitic carbon nitride (Fig. 3b) was successfully combined with the MOF, as shown in Fig. 3c, which was further validated by the presence of both Fe and N in the EDX data of the composite material (Fig. 3d and Table S1†). Interestingly, the TEM images of O-g-C$_3$N$_4$/MIL-53(Fe) (Fig. 3e−g) disclose the appearance of multi-walled nanotubes with the onion-like walls

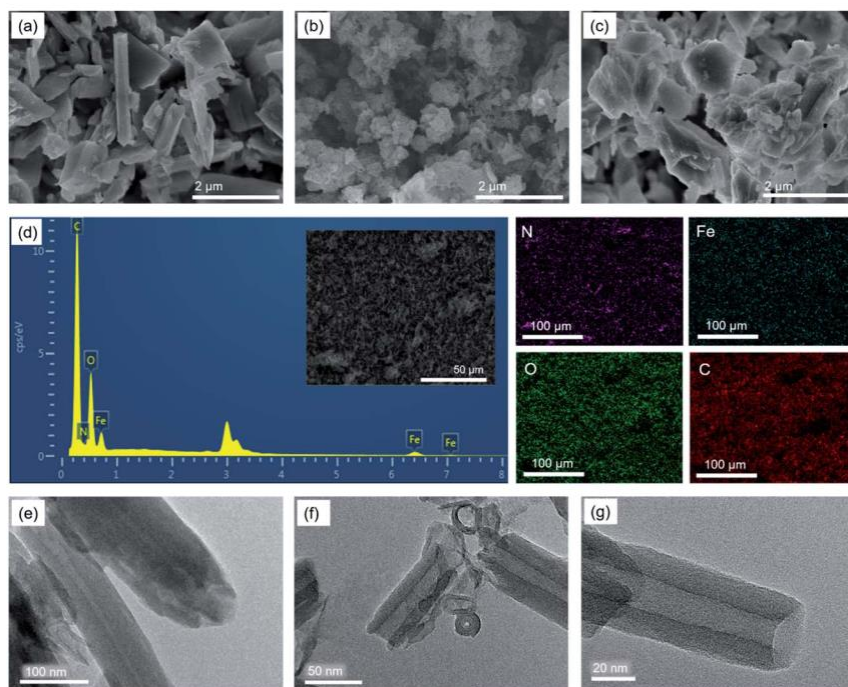

Fig. 3 SEM images of (a) MIL-53(Fe), (b) g-C$_3$N$_4$ and (c) the O-g-C$_3$N$_4$/MIL-53(Fe) composite. (d) EDX spectra and elemental mapping of the O-g-C$_3$N$_4$/MIL-53(Fe) composite. (e−g) TEM images of the O-g-C$_3$N$_4$/MIL-53(Fe) composite.

annealing instantly under the beam, which is due to the integration of the exfoliated graphitic carbon nitride nanosheets (Fig. S1a and b†) into the MOF mate-rial. Additional TEM images of this composite sample can be seen in Fig. S1d−h.† The novel porous structure of O-g-C$_3$N$_4$/MIL-53(Fe) was further examined using a gas sorption technique. As shown in Fig. 4a and Table S2,† a hysteresis clearly emerges in the nitrogen isotherm of O-g-C$_3$N$_4$/MIL-53(Fe), followed by a slightly larger surface area S$_{BET}$ (28.5 m^2 g^{-1}) and pore volume V$_p$ (0.136 cm^3 g^{-1}) this composite material compared to the separate MIL-53(Fe) (S$_{BET}$ ¼ 20.4 m^2 g^{-1} and V$_p$ ¼ 0.052 cm^3 g^{-1}) and O-g-C$_3$N$_4$ (S$_{BET}$ ¼ 22.1 m^2 g^{-1} and V$_p$ ¼ 0.117 cm^3 g^{-1}) components. Fig. 4b indicates that extra mesopores with sizes of 9 and 22 nm were observed in the Barrett−Joyner−Halenda (BJH) pore size distribution, confirming the presence of nanotubes in the O-g-C$_3$N$_4$/MIL-53(Fe) composite material.

3.3. Optical and photoelectrochemical properties

The optical properties of the g-C$_3$N$_4$, O-g-C$_3$N$_4$ and O-g-C$_3$N$_4$/MIL-53(Fe) samples were assessed using ultraviolet-visible diffuse reflectance spectroscopy (UV-Vis DRS), as seen in Fig. 5a. For the pristine g-C$_3$N$_4$, a band edge is observed at 475 nm, which is consistent with previous reports.[61] In the case of O-g-C$_3$N$_4$, the absorption edge shifts to a longer wavelength, indicating enhanced visible-light absorption in this sample. A small peak at 500 nm found in O-g-C$_3$N$_4$/MIL-53(Fe) is attributed to the electronic transition of the d-orbitals in Fe^{3+}, with a similar result for Fe$_2$Ni-MIL-88B previously reported by Vuong et al.[62,63] Here, the estimated absorption edge for O-g-C$_3$N$_4$/MIL-53(Fe) is 540 nm, which is significantly higher than those for g-C$_3$N$_4$ (475 nm) and O-g-C$_3$N$_4$ (486 nm). The corresponding bandgap energies (E$_g$) of these samples were calculated using the Kubelka−Munk equation[64] (see ESI†) and listed in Table 1. Photoluminescence spectroscopy (PL) was implemented to investigate the carrier separation efficiency of g-C$_3$N$_4$, O-g-C$_3$N$_4$ and O-g-C$_3$N$_4$/MIL-53(Fe). The higher the intensity of the emission peak, the more rapid the recombination of the photoexcited electron− hole pairs.[65] As can be seen in Fig. 5b, a PL emission peak between 400 and 500 nm is observed in all samples with the highest intensity observed in g-C$_3$N$_4$, followed by O-g-C$_3$N$_4$ and O-g-C$_3$N$_4$/MIL-53(Fe), which is in good agreement with
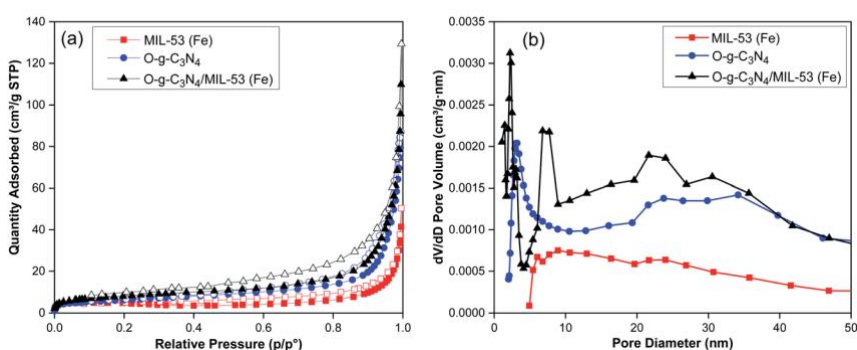

Fig. 4 (a) N$_2$ adsorption−desorption isotherms and (b) pore size distribution of MIL-53(Fe), O-g-C$_3$N$_4$ and the O-g-C$_3$N$_4$/MIL-53(Fe) composite.
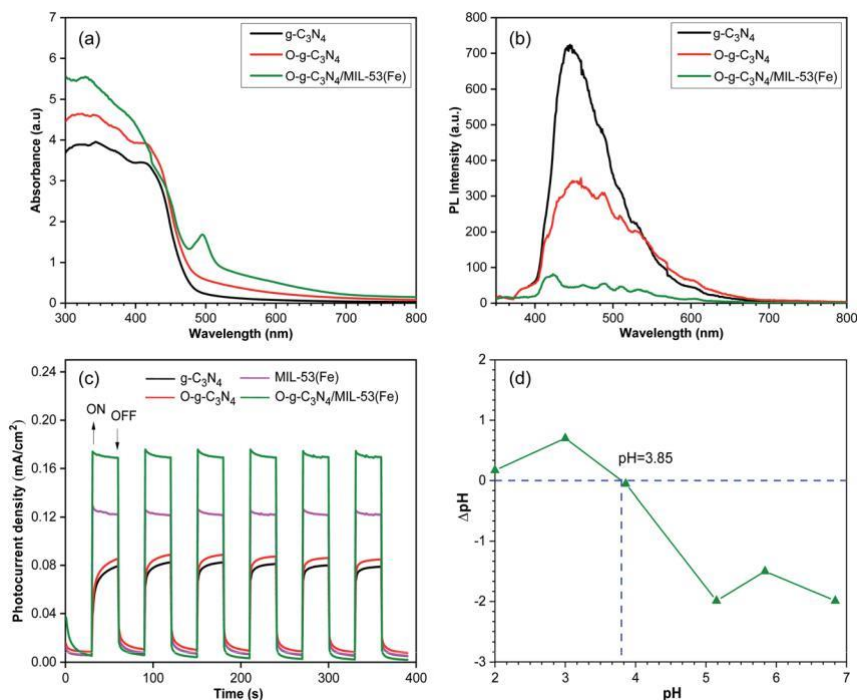
Fig. 5 (a) UV-Vis diffuse reflectance spectra and (b) photoluminescence spectra of g-C3N4, O-g-C3N4 and the O-g-C3N4/MIL-53(Fe) composite. (c) Transient photocurrent response of g-C3N4, O-g-C3N4, MIL-53(Fe) and the O-g-C3N4/MIL-53(Fe) composite. (d) Point of zero charge of O-g-C3N4/MIL-53(Fe).

Table 1 Optical properties of g-C3N4, O-g-C3N4 and the O-g-N4/MIL-53(Fe) composite

Sample	Absorption edge (nm)	Bandgap energy (eV)
g-C3N4	475	2.60
O-g-C3N4	486	2.55
O-g-C3N4/MIL-53(Fe)	540	2.30

the analysis of the UV-Vis DRS. These results indicate the enhanced separation rates of the photoinduced electron–hole pairs, which is due to the effective charge transfer across the interface and the reduced charge transport distance at the heterojunction in the composite material.

Transient photocurrent (TPC) response analysis was carried out to investigate the photoelectrochemical properties of g-C3N4, O-g-C3N4, MIL-53(Fe) and O-g-C3N4/MIL-53(Fe). As shown in Fig. 5c, all of the samples exhibit rapid photocurrent responses when the light is turned on and off for 6 cycles within 400 s. The photocurrent remains relatively stable over the 6 cycles, indicating the good reproducibility of the samples during the irradiation process. Further observation shows that the photocurrent of O-g-C3N4/MIL-53(Fe) (0.17 mA cm^{-2}) is significantly higher than those of MIL-53(Fe) (0.12 mA cm^{-2}), O-g-C3N4 (0.09 mA cm^{-2})

and g-C_3N_4 (0.08 mA cm^{-2}), demonstrating that the separation efficiency of the photoinduced electron–hole pairs in O-g-C_3N_4/MIL-53(Fe) is improved due to the unique interfacial charge transfer at the heterojunction. As compared to pristine MIL-53(Fe), O-g-C_3N_4/MIL-53(Fe) exhibits higher photocurrent intensity, as the multi-walled nanotube structure exposes more active sites to restrict the recombination. In addition, the point of zero charge (pzc) was measured for the O-g-C_3N_4/MIL-53(Fe) composite under different pH conditions to investigate the surface charge of this sample. It is widely known that particles are positively charged at pH values below the pzc and negatively charged above this point.[66] Fig. 5d shows that the DpH values (DpH ¼ pH$_o$ pH$_f$) are negative over nearly the entire pH region studied and the pzc of O-g-C_3N_4/MIL-53(Fe) was determined to be 3.85. The various surface charges under different pH conditions are due to the diverse chemical interactions in O-g-C_3N_4, where the amine groups, including C– NH_2, C_2–NH and C_3N, can exhibit protonation and deprotonation in aqueous suspensions.[67]

3.4. Photocatalytic testing

The photocatalytic performances of the synthesised samples were investigated by the removal of RR 195 and RY 145 under natural light. A pre-test experiment was carried out before introducing the catalysts (Fig. S4a†), confirming that almost no RR 195 was degraded (less than 2.5%) under sunlight over 4 h. Fig. 6a shows that
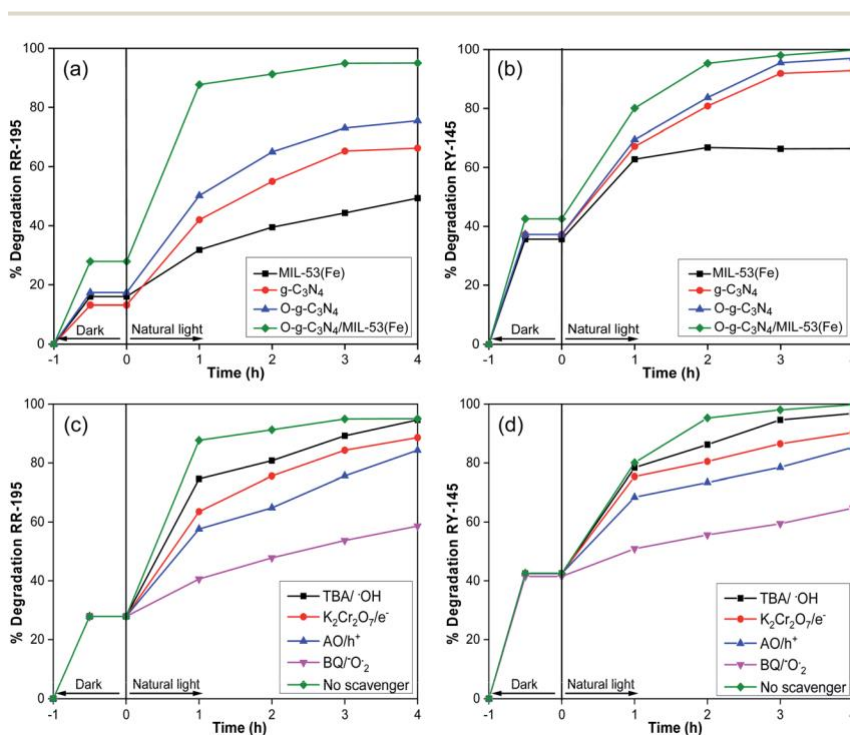

Fig. 6 Photocatalytic degradation of (a) RR 195 and (b) RY 145 using g-C_3N_4, O-g-C_3N_4, MIL-53(Fe) and O-g-C_3N_4/MIL-53(Fe). The active species trapping experiments for degradation of (c) RR 195 and (d) RY 145 over the O-g-C_3N_4/MIL-53(Fe) photocatalyst.

the degradations of RR 195 at the adsorption–desorption equilibrium point using MIL-53(Fe), g-C$_3$N$_4$, O-g-C$_3$N$_4$ and O-g-C$_3$N$_4$/MIL-53(Fe) are 16%, 13%, 17% and 28%, respectively. A er 4 h of illumination, the O-g-C$_3$N$_4$/MIL-53(Fe) composite shows a relatively high photocatalytic efficiency for RR 195 degradation (95.1% compared to 49%, 66% and 76% using MIL-53(Fe), g-C$_3$N$_4$ and O-g-C$_3$N$_4$, respectively). A similar pattern is shown for the degradation of RY 145 (Fig. 6b), where the catalytic activity of the samples a er 4 h follows the order of MIL-53(Fe) (66%) < g-C$_3$N$_4$ (93%) < O-g-C$_3$N$_4$ (97%) < O-g-C$_3$N$_4$/MIL-53(Fe) (99%). The higher degradation efficiency of O-g-C$_3$N$_4$ compared to g-C$_3$N$_4$ is due to the defect formation in the graphitic framework upon oxygen doping (as shown previously in the PXRD result) which generates more excited electron–holes and increases the visible light absorption.[31,32,50] This result is in good agreement with the PL and TPC results discussed above. The highest photocatalytic activity observed in O-g-C$_3$N$_4$/MIL-53(Fe) is due to the heterojunction structure between O-g-C$_3$N$_4$ and MIL-53(Fe), along with the multi-walled nanotube structure, which can accelerate the charge transfer across the interface and shorten the charge transport distance, thus enhancing the separation efficiency of the photochemical electron–hole pairs in this composite material. Fig. S4b† shows that O-g-C$_3$N$_4$ was inactive in the dark, confirming the role of light in the removal of the anion dyes. The photo-degradation of RY-195 using O-g-C$_3$N$_4$ was also repeated using a xenon lamp of 500 W (Fig. S4c†) to validate the stability of the solar radiation during the experiment, and indicated that no significant variation was observed between these two light sources. This result suggests the possible use of a sunlight simulator when the natural source is inaccessible.

The effect of O-g-C$_3$N$_4$/MIL-53(Fe) on the decomposition of RR 195 and RY 145 was further investigated by varying the initial concentration of the anionic dyes (30–70 ppm) and the amount of catalyst (25–75 mg) used in the photocatalytic reaction. Fig. S3a and b† show that a higher catalyst loading of up to 50 mg can facilitate the improved degradation efficiency for both the RR 195 and RY 145 dyes. When more catalyst was loaded a er this point, the degradation remained almost unchanged, demonstrating that the optimal efficiency to remove 50 ppm anionic dyes from water can be achieved using 50 mg of O-g-C$_3$N$_4$/MIL-53(Fe). The initial concentration of the anionic dyes was also a factor, as demonstrated in Fig. S3c and d.† A er reacting for 4 h under natural light using 50 mg of O-g-C$_3$N$_4$/ MIL-53(Fe), the anionic dyes can be completely degraded in the contaminated water containing 30 ppm of RR 195 or 70 ppm of RY 145. Looking at the benchmark data (Table S3†), the performance of O-g-C$_3$N$_4$/MIL-53(Fe) in this study is comparable to or far outperforms other materials such as commercial titanium oxide catalysts,[68] O-g-C$_3$N$_4$/H-ZSM-5 (ref. 35) and the nano Fe-BTC/GO composite[69] which were tested in similar conditions.

Here, trapping experiments were performed to identify the active species and understand the mechanism of the photocatalytic process over O-g-C$_3$N$_4$/MIL-53(Fe). As shown in Fig. 6c and d, the decomposition rate of RR 195 and RY 145 decreases in the presence of tert-butyl alcohol (TBA), potassium dichromate (K$_2$Cr$_2$O$_7$), ammonium oxalate monohydrate (AO) and 1,4-benzoquinone (BQ), indicating that hydroxyl radicals (cOH), electrons (e), holes (h$^+$) and superoxide radicals (cO$_2$) were formed during the photocatalysis. A significant reduction in the degradation is observed a er the introduction of BQ and AO compared to K$_2$Cr$_2$O$_7$ and TBA, demonstrating that the superoxide radicals and holes act as the
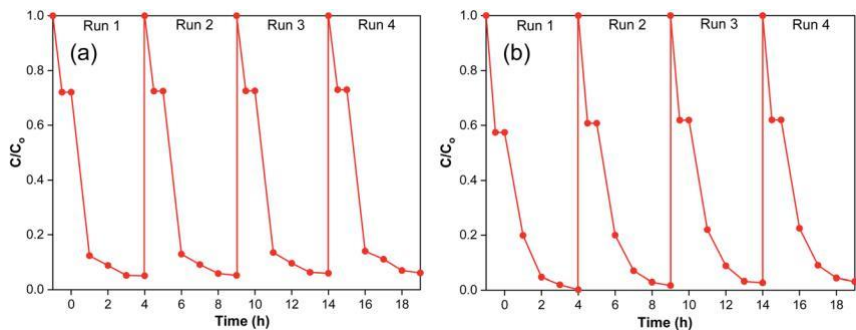
Fig. 7 Recyclability of O-g-C$_3$N$_4$/MIL-53(Fe) in the photodegradation of (a) RR 195 and (b) RY 145.

primary active species in O-g-C$_3$N$_4$/MIL-53(Fe) photodegradation. This result can be used to explain the enhanced photocatalytic performance of the composite material, in which the intrinsic electronic structure and multi-walled nanotube morphology were induced to enhance the electron migration efficiency and decrease the recombination possibility of the electron–hole pairs.

The recyclability properties of O-g-C$_3$N$_4$/MIL-53(Fe) in the photodegradation of RR 195 and RY 145 were also evaluated (Fig. 7), showing that the catalytic activity of this sample exhibits only a minor change a er four consecutive tests (from 95% to 94% for RR 195 and from 99% to 97% for RY 145) which might be due to the loss of the catalyst during filtration after each cycle. The PXRD patterns (Fig. S5†) con rm that the crystallinity was still retained a er four cycles, demonstrating the excellent stability of the synthesised O-g-C$_3$N$_4$/MIL-53(Fe) composite material during the photodegradation of anionic dyes.

4.   Conclusions

In this study, a composite formed of a complex graphitic carbon nitride and a MOF material was successfully synthesised from O-g-C$_3$N$_4$ and MIL-53(Fe) using a facile hydrothermal approach. The novel multi-walled nanotube structure of O-g-C$_3$N$_4$/MIL-53(Fe) with intrinsic electronic modulation efficiently inhibited the recombination of the electron–hole pairs in photocatalysis. The composite material exhibited a narrow bandgap energy (2.30 eV), a high photocurrent intensity (0.17 mA cm^2) and enhanced catalytic performance in the removal of two commercial textile azo-dyes (RR 195 and RY 145) under solar irradiation. The recycled PET used for the synthesis of MIL-53(Fe) in this study would allow for plastic waste to be economically valuable again which would protect wildlife and the environment from further pollution.

Author contributions

X. N. P. and H. V. D. conceived and designed the experiments. X. N. P. directed the project. H. V. D wrote the paper. H. T. N. performed the sample preparation and photodegradation testing. J. C. E. and S. G. performed the TEM and XPS

experiments, respectively. V. P. T. and S. R. H. revised the manuscript. All authors have contributed to the improvement of this article.

Conflicts of interest

There are no conflicts of interest to declare.

Acknowledgements

References

1 F. Li, Y. Dong, W. Kang, B. Cheng and G. Cui, Appl. Surf. Sci., 2017, **404**, 206–215.

2 E. Khalilzadeh Shirazi, J. W. Metzger, K. Fischer and A. H. Hassani, Colloids Surf., A, 2020, **598**, 124807.

3 A. Soleimani-Gorgani and J. A. Taylor, Dyes Pigm., 2008, **76**, 610–623.

4 S. Papi´c, N. Koprivanac, A. Lonˇcari´c Boˇzi´c and A. Meteˇs, Dyes Pigm., 2004, **62**, 291–298.

5 M. Vakili, M. Rafatullah, B. Salamatinia, A. Z. Abdullah, M. H. Ibrahim, K. B. Tan, Z. Gholami and P. Amouzgar, Carbohydr. Polym., 2014, **113**, 115–130.

6 I. Arslan and I. A. Balcioglu, Color. Technol., 2001, **117**, 38–42.

7 M. Ozacar and I. A. ¸Sengil, J. Hazard. Mater., 2003, **98**, 211–224.

8 I. Ali, O. M. L. Alharbi, Z. A. Alothman and A. Y. Badjah, Photochem. Photobiol., 2018, **94**, 935–941.

9 R. L´opez Cisneros, A. Gutarra Espinoza and M. I. Litter, Chemosphere, 2002, **48**, 393–399.

10 Y. Li, W. Xie, X. Hu, G. Shen, X. Zhou, Y. Xiang, X. Zhao and P. Fang, Langmuir, 2010, **26**, 591–597.

11 C. Tian, Q. Zhang, A. Wu, M. Jiang, B. Jiang and H. Fu, Chem. Commun., 2012, **48**, 2858–2860.

12 W. Konicki, M. Aleksandrzak, D. Moszynski´ and E. Mijowska, J. Colloid Interface Sci., 2017, **496**, 188–200.

13 F. Çiçek, D. Ozer,¨ A. Ozer¨ and A. Ozer,¨ J. Hazard. Mater., 2007, **146**, 408 416.

14 J. P´erez-Calder´on, M. V. Santos and N. Zaritzky, J. Environ. Chem. Eng., 2018, **6**, 6749–6760.

15 S. D. Ashra , S. Rezaei, H. Forootanfar, A. H. Mahvi and M. A. Faramarzi, Int. Biodeterior. Biodegrad., 2013, **85**, 173–181.

16 H. Kamani, G. H. Safari, G. Asgari and S. D. Ashra , Data in Brief, 2018, **18**, 80–86.

17 X. N. Pham, M. B. Nguyen, H. S. Ngo and H. V. Doan, J. Ind. Eng. Chem., 2020, **90**, 358–370.

18 X. N. Pham, B. M. Nguyen, H. T. Thi and H. Van Doan, Adv. Powder Technol., 2018, **29**, 1827–1837.

19 X. N. Pham, D. T. Pham, H. S. Ngo, M. B. Nguyen and H. V. Doan, Chem. Eng. Commun., 2020, 1–14.

20 V. H. T. Nguyen, M. N. Nguyen, T. T. Truong, T. T. Nguyen, H. V. Doan and X. N. Pham, J. Nanomater., 2020, **2020**, 1–12.

21 X. N. Pham, M. B. Nguyen and H. V. Doan, Adv. Powder Technol., 2020, **31**, 3351–3360.

22 S. Cao, J. Low, J. Yu and M. Jaroniec, Adv. Mater., 2015, **27**, 2150–2176.

23 A. Mishra, A. Mehta, S. Basu, N. P. Shetti, K. R. Reddy and T. M. Aminabhavi, Carbon, 2019, **149**, 693–721.

24 L. Wang, G. Zhou, Y. Tian, L. Yan, M. Deng, B. Yang, Z. Kang and H. Sun, Appl. Catal., B, 2019, **244**, 262–271.

25 J. Liu and B. Cheng, Appl. Surf. Sci., 2018, **430**, 348–354.

26 Q. Zhong, H. Lan, M. Zhang, H. Zhu and M. Bu, Ceram. Int., 2020, **46**, 12192–12199.

27 J. Zhang, Y. Wang, J. Jin, J. Zhang, Z. Lin, F. Huang and J. Yu, ACS Appl. Mater. Interfaces, 2013, **5**, 10317–10324.

28 W. Jiang, W. Luo, J. Wang, M. Zhang and Y. Zhu, J. Photochem. Photobiol., C, 2016, **28**, 87–115.

29 S. Patnaik, S. Martha and K. M. Parida, RSC Adv., 2016, **6**, 46929–46951.

30 S. Patnaik, D. P. Sahoo and K. Parida, Carbon, 2021, **172**, 682–711.

31 F. Ling, W. Li and L. Ye, Appl. Surf. Sci., 2019, **473**, 386–392.

32 L. Yang, J. Huang, L. Shi, L. Cao, Q. Yu, Y. Jie, J. Fei, H. Ouyang and J. Ye, Appl. Catal., B, 2017, **204**, 335–345.

33 Y. P. Zhu, T. Z. Ren and Z. Y. Yuan, ACS Appl. Mater. Interfaces, 2015, **7**, 16850–16856.

34 J. Li, B. Shen, Z. Hong, B. Lin, B. Gao and Y. Chen, Chem. Commun., 2012, **48**, 12017–12019.

35 X. N. Pham, H. T. Nguyen, T. N. Pham, T. T. B. Nguyen, M. B. Nguyen, V. T. T. Tran and H. V. Doan, J. Taiwan Inst. Chem. Eng., 2020, **114**, 91–102.

36 K. Dai, L. Lu, C. Liang, G. Zhu, Q. Liu, L. Geng and J. He, Dalton Trans., 2015, **44**, 7903–7910.

37 H. T. Ren, S. Y. Jia, S. H. Wu, T. H. Zhang and X. Han, Mater. Lett., 2015, **142**, 15–18.

38 L. Liu, Y. Qi, J. Lu, S. Lin, W. An, Y. Liang and W. Cui, Appl. Catal., B, 2016, **183**, 133–141.

39 H. V. Doan, H. Amer Hamzah, P. Karikkethu Prabhakaran, C. Petrillo and V. P. Ting, Nano-Micro Lett., 2019, **11**, 54.

40 H. V. Doan, A. Sartbaeva, J. C. Eloi, S. A. Davis and V. P. Ting, Sci. Rep., 2019, **9**, 10887.

41 H. V. Doan, Y. Fang, B. Yao, Z. Dong, T. J. White, A. Sartbaeva, U. Hintermair and V. P. Ting, ACS Sustainable Chem. Eng., 2017, **5**, 7887–7893.

42 H. V. Doan, F. Cheng, T. Dyirakumunda, M. R. J. Elsegood, J. Chin, O. Rowe, C. Redshaw and V. P. Ting, Crystals, 2020, **10**, 17.

43 C. C. Wang, X. H. Yi and P. Wang, Appl. Catal., B, 2019, 247, 24–48.

44 W. Huang, N. Liu, X. Zhang, M. Wu and L. Tang, Appl. Surf. Sci., 2017, 425, 107–116.

45 F. Zhao, Y. Liu, S. Ben Hammouda, B. Doshi, N. Guijarro, X. Min, C. J. Tang, M. Sillanp¨a¨a, K. Sivula and S. Wang, Appl. Catal., B, 2020, 272, 119033.

46 B. Liu, Y. Wu, X. Han, J. Lv, J. Zhang and H. Shi, J. Mater. Sci.: Mater. Electron., 2018, 29, 17591–17601.

47 X. Li, Y. Pi, L. Wu, Q. Xia, J. Wu, Z. Li and J. Xiao, Appl. Catal., B, 2017, 202, 653–663.

48 D. Wang and Z. Li, Res. Chem. Intermed., 2017, 43, 5169–5186.

49 Q. Xia, H. Wang, B. Huang, X. Yuan, J. Zhang, J. Zhang, L. Jiang, T. Xiong and G. Zeng, Small, 2019, 15, 1803088.

50 Z. Wei, M. Liu, Z. Zhang, W. Yao, H. Tan and Y. Zhu, Energy Environ. Sci., 2018, 11, 2581–2589.

51 S. C. Yan, Z. S. Li and Z. G. Zou, Langmuir, 2009, 25, 10397–10401.

52 Y. Fu, J. Zhu, C. Hu, X. Wu and X. Wang, Nanoscale, 2014, 6, 12555–12564.

53 J. P. S. Mowat, V. R. Seymour, J. M. Griffin, S. P. Thompson, A. M. Z. Slawin, D. Fairen-Jimenez, T. Duren,¨ S. E. Ashbrook and P. A. Wright, Dalton Trans., 2012, 41, 3937–3941.

54 P. Horcajada, C. Serre, G. Maurin, N. A. Ramsahye, F. Balas, M. Vallet-Reg´ı, M. Sebban, F. Taulelle and G. F´erey, J. Am. Chem. Soc., 2008, 130, 6774–6780.

55 L. Ai, C. Zhang, L. Li and J. Jiang, Appl. Catal., B, 2014, 148–149, 191–200.

56 T. F. Yeh, C. Y. Teng, S. J. Chen and H. Teng, Adv. Mater., 2014, 26, 3297–3303.

57 Y. Zhang, J. Liu, G. Wu and W. Chen, Nanoscale, 2012, 4, 5300–5303.

58 F. Wei, Y. Liu, H. Zhao, X. Ren, J. Liu, T. Hasan, L. Chen, Y. Li and B. L. Su, Nanoscale, 2018, 10, 4515–4522.

59 J. Huang, H. Wang, H. Yu, Q. Zhang, Y. Cao and F. Peng, ChemSusChem, 2020, 13, 5041–5049.

60 Y. Gao, S. Li, Y. Li, L. Yao and H. Zhang, Appl. Catal., B, 2017, 202, 165–174.

61 A. Akhundi and A. Habibi-Yangjeh, Ceram. Int., 2015, 41, 5634–5643.

62 G. T. Vuong, M. H. Pham and T. O. Do, Dalton Trans., 2013, 42, 550–557.

63 G. T. Vuong, M. H. Pham and T. O. Do, CrystEngComm, 2013, 15, 9694–9703.

64 P. Kubelka and F. Munk, Z. Tech. Phys., 1931, 12, 593–601.

65 H. Shi, G. Chen, C. Zhang and Z. Zou, ACS Catal., 2014, 4, 3637–3643.

66 N. Fiol and I. Villaescusa, Environ. Chem. Lett., 2009, 7, 79–84.

67 B. Zhu, P. Xia, W. Ho and J. Yu, Appl. Surf. Sci., 2015, 344, 188–195.

68 B. Chl´adkov´a, E. Evgenidou, L. Kv´ıtek, A. Panˇaˇcek, R. Zboˇril, P. Kov´aˇr and D. Lambropoulou, Environ. Sci. Pollut. Res., 2015, 22, 16514–16524.

69 H. T. Vu, M. B. Nguyen, T. M. Vu, G. H. Le, T. T. T. Pham, T. Duy Nguyen and T. A. Vu, Top. Catal., 2020, 63, 1046–1055.